

Physical properties of the first spectroscopically confirmed red supergiant stars in the Sculptor Group galaxy NGC 55

L. R. Patrick,^{1,2,3*} C. J. Evans,^{3,4} B. Davies,⁵ R-P. Kudritzki,^{6,7} A. M. N. Ferguson,³ M. Bergemann,⁸ G. Pietrzyński,^{9,10} and O. Turner³

¹*Instituto de Astrofísica de Canarias, E-38205 La Laguna, Tenerife, Spain*

²*Universidad de La Laguna, Dpto. Astrofísica, E-38206 La Laguna, Tenerife, Spain*

³*Institute for Astronomy, University of Edinburgh, Royal Observatory Edinburgh, Blackford Hill, Edinburgh EH9 3HJ, UK*

⁴*UK Astronomy Technology Centre, Royal Observatory Edinburgh, Blackford Hill, Edinburgh EH9 3HJ, UK*

⁵*Astrophysics Research Institute, Liverpool John Moores University, Liverpool Science Park ic2, 146 Brownlow Hill, Liverpool L3 5RF, UK*

⁶*Institute for Astronomy, University of Hawaii, 2680 Woodlawn Drive, Honolulu, HI, 96822, USA*

⁷*University Observatory Munich, Scheinerstr. 1, D-81679, Munich, Germany*

⁸*Max-Planck Institute for Astronomy, D-69117, Heidelberg, Germany*

⁹*Universidad de Concepción, Departamento de Astronomía, Casilla 160-C, Concepción, Chile*

¹⁰*Nicolaus Copernicus Astronomical Centre, Polish Academy of Sciences, Bartycka 18, PL-00-716 Warszawa, Poland*

Accepted XXX. Received YYY; in original form ZZZ

ABSTRACT

We present *K*-band Multi-Object Spectrograph (KMOS) observations of 18 Red Supergiant (RSG) stars in the Sculptor Group galaxy NGC 55. Radial velocities are calculated and are shown to be in good agreement with previous estimates, confirming the supergiant nature of the targets and providing the first spectroscopically confirmed RSGs in NGC 55. Stellar parameters are estimated for 14 targets using the *J*-band analysis technique, making use of state-of-the-art stellar model atmospheres. The metallicities estimated confirm the low-metallicity nature of NGC 55, in good agreement with previous studies. This study provides an independent estimate of the metallicity gradient of NGC 55, in excellent agreement with recent results published using hot massive stars. In addition, we calculate luminosities of our targets and compare their distribution of effective temperatures and luminosities to other RSGs, in different environments, estimated using the same technique.

Key words: stars: abundances – (stars:) supergiants – (galaxies:) NGC 55

1 INTRODUCTION

The Sculptor “Group” is a filament-shaped group of galaxies extending over ~ 5 Mpc along the line of sight (Jensen et al. 1998; Karachentsev et al. 2003), containing three subgroups (Karachentsev et al. 2003) centred around NGC 253 ($d \sim 4$ Mpc), NGC 7793 ($d \sim 4$ Mpc) and NGC 300 ($d \sim 2$ Mpc). NGC 55 is a member of the nearest subgroup that also contains NGC 300 and a number of dwarf galaxies. As one can resolve individual bright stars in these galaxies, the Sculptor Group provides us with a fantastic laboratory to investigate stellar and galactic evolution beyond the Local Group.

Table 1 summarises the observational properties of NGC 55, which has an asymmetric and complicated morphology, due to its high inclination (up to 80° ; Hummel et al.

1986; Westmeier et al. 2013). de Vaucouleurs (1961) classified it as an LMC-like barred spiral galaxy (SB(s)m), where the bar is seen along the line of sight, prompting various claims that it is an edge-on analogue of the LMC. Figure 1 shows NGC 55 and its complicated morphology, where one can see the edge-on disk (along the major axis of the galaxy) and the brighter central part of the galaxy, which represents the head of the bar. In addition to NGC 55 being orientated nearly edge on, there are many star-formation features extending from the disk-bar system such as giant H II regions and supergiant filaments and shells, which are thought to allow ionising radiation to be transported to the halo (Ferguson et al. 1996).

The ionised gas morphology of NGC 55, as well as its known population of massive hot stars (Castro et al. 2008, 2012), points to a recent history of intense star formation. The infrared luminosity of NGC 55 implies a star-formation rate of $0.22 M_\odot \text{yr}^{-1}$ (Engelbracht et al. 2004) and is dom-

* E-mail: lpatrick@iac.es

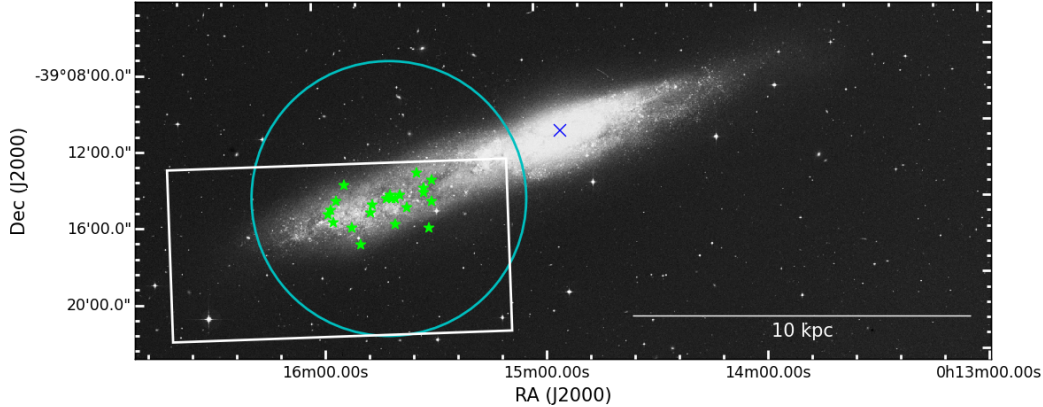


Figure 1. Digital sky survey image of NGC 55 with the KMOS targets overlaid in green and the relevant footprint from the Araucaria Project (Pietrzyński et al. 2006) shown as a white rectangle. The 7' diameter field of view of KMOS is indicated by the blue circle. The centre of NGC 55, as defined by the Two Micron All Sky Survey (2MASS; Skrutskie et al. 2006), is shown as a blue cross.

Table 1. Basic properties of NGC 55.

Property	Value	Reference
Classification	SB(s)m	de Vaucouleurs et al. (1991)
α (J2000)	00 ^h 14 ^m 53.602 ^s	Skrutskie et al. (2006)
δ (J2000)	-39 11 47.86	Skrutskie et al. (2006)
Distance	2.34 ± 0.11 Mpc	Kudritzki et al. (2016)
Inclination	$78 \pm 4^\circ$	Puche et al. (1991), Westmeier et al. (2013)
Radial velocity	131 ± 2 km s ⁻¹	Westmeier et al. (2013)

inated by a bright central region and disk emission, which supports the hypothesis of recent star formation. Here we present the first spectroscopic study of red supergiant stars (RSGs) in NGC 55, with the objective of providing an independent check on the metallicity estimates from blue supergiants (BSGs) and H II regions.

From galaxy mass-metallicity relations, the metal content of NGC 55 was expected to be LMC-like, which is supported by Castro et al. (2012), who measured metallicities of 12 BSGs using optical spectroscopy and found a mean metallicity $[Z] = \log(Z/Z_\odot) = -0.40 \pm 0.13$ dex. In addition, the literature contains several metallicity measurements from H II regions across the disk of NGC 55, finding a large spread of metallicities (-0.6 to -0.2 – assuming a solar-like α/Fe ; Webster & Smith 1983; Stasińska et al. 1986; Zaritsky et al. 1994; Tüllmann et al. 2003; Castro et al. 2012)

In addition, the BSG work of Castro et al. (2012) has recently been taken further by Kudritzki et al. (2016), who analysed ~ 60 BSGs across a large spatial extent of NGC 55. These authors found a central metallicity of $[Z] = -0.37 \pm 0.03$ dex, in good agreement with Castro et al. (2012). Interestingly, these authors also found evidence for a metallicity gradient of -0.22 ± 0.06 dex/ R_{25} , the first such evidence in this galaxy. On the other hand, Magrini et al. (2017) estimate abundances from 25 H II regions within NGC 55 finding no evidence for an abundance gradient. Therefore, it is important that we obtain independent estimates of metal-

licities in NGC 55 to provide insight into this potential discrepancy.

Even though the hot massive-star population of NGC 55 has been explored, there are currently no confirmed RSGs in NGC 55, although Davidge (2005) noted that the near-IR colour–magnitude diagram (CMD) of fields within the disk reveal RSG candidates. The current study represents the first quantitative analysis of RSGs in NGC 55 and it will provide an independent estimate of the metallicity of the young stellar population within this galaxy.

In recent years, moderate resolution spectroscopy has been shown to be a useful tool to determine the physical parameters of RSGs (Davies et al. 2010, 2015). In this context, the *K*-band Multi-Object Spectrograph (KMOS; Sharples et al. 2013) on the Very Large Telescope (VLT), has been used to explore the chemical evolution of external galaxies using RSGs as cosmic abundances probes. This analysis makes use of state-of-the-art stellar model atmospheres including departures from the assumption of local thermodynamic equilibrium (LTE) for the strongest absorption lines in a spectral window in the *J*-band (Bergemann et al. 2012, 2013, 2015). The first application of this technique with KMOS was by Patrick et al. (2015) who investigated RSGs in NGC 6822 ($d \sim 0.5$ Mpc). Building on this initial study we have explored the RSG population in several external galaxies within and beyond the Local Group of galaxies.

In addition to applying this technique to individual RSGs, we can estimate metallicities of more distant star clusters, in which the integrated near-IR flux is dominated by the contribution from RSGs (Gazak et al. 2013). Lardo et al. (2015) applied this technique to three super star clusters in NGC 4038, one of the Antennae galaxies. Further ahead, with a near-IR multi-object spectrograph on a 30-m class telescope, Evans et al. (2011) demonstrated that individual metallicities of RSGs can be estimated at distances of tens of Mpc and, using the integrated-light analysis, at distances of hundreds of Mpc with clusters.

In this paper we present the analysis of KMOS observations of RSGs in NGC 55. Sections 2 and 3 detail the target selection, observations and data reduction. In Section 4 the main results of the paper are presented and discussed, which

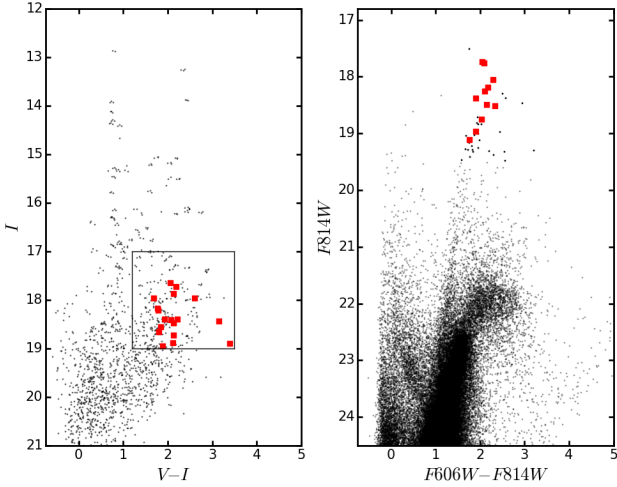


Figure 2. Colour-magnitude diagrams used for target selection. Left-hand panel: ground-based photometry from Pietrzyński et al. (2006) for the area highlighted in Figure 1. The black box was used to select candidate RSGs ($17 < I < 19$, $1.2 < V - I < 3.5$). Right-hand panel: overlapping *HST* photometry of part of the KMOS field from Dalcanton et al. (2009). Observed targets are highlighted with red squares.

include radial-velocity estimates – confirming their membership of NGC 55, and by inference nature as supergiants – and the estimates of the physical parameters of our targets. The conclusions of the study are summarised in Section 5.

2 TARGET SELECTION

Targets were selected for spectroscopy based on their optical photometry from the Araucaria Project (Pietrzyński et al. 2006), where the footprint of the relevant CCD is highlighted with a large white rectangle in Figure 1. This is ground-based data taken with the 1.3 m Warsaw Telescope where the pixel scale was $0''.25$ and the typical seeing conditions were $1''.0$.

The optical CMD used to select targets is displayed in the left-hand panel of Figure 2, where the RSG candidates are within the black box and the observed targets are highlighted in red.

Candidate RSGs are defined as having $17 < I < 19$ and $1.2 < V - I < 3.5$. The magnitude limits were chosen to give $S/N \sim 100$ for the requested exposure times of the observations (cf. Gazak et al. 2015, which used similar selection criteria for NGC 300), however the requested programme was not fully realised and hence the final S/N of the spectra is somewhat lower. The $V - I$ colour limit is chosen to avoid potential Galactic contamination at $V - I \sim 0.95$. All stars that meet these criteria are defined as candidate RSGs and the final target selection was performed by analysing the spatial location of the candidates and selecting those which traced the disk population of NGC 55 (see Figure 1).

In addition to the ground-based photometry available, the ACS Nearby Galaxy Survey Treasury (ANGST; Dalcanton et al. 2009) project has publicly-available photometry for several fields within the disk of NGC 55, although we

preferred use of the ground-based data for its more comprehensive coverage in the south-east part of the NGC 55 disk. A $F814W$, $F606W - F814W$ CMD is shown in the right-hand panel of Figure 2 for the ACS ANGST field which contains 11 of our KMOS targets, highlighted in red. Given the smaller spatial coverage of the *HST* ACS field, the expected number of Galactic contaminants is corresponding smaller. As a result of their cool temperatures and extreme luminosities, RSGs should exist in a “plume” at the tip of a structure of cool stars in the $F606W - F814W$, $F814W$ CMD. This compares well to the location (in colour–magnitude parameter space) of confirmed RSGs in NGC 300 (Gazak et al. 2015).

3 OBSERVATIONS AND DATA REDUCTION

The data were obtained as part of the KMOS Guaranteed Time Observations (GTO, 092.B-0088) to investigate stellar metallicities in NGC 300 and NGC 55. We observed one KMOS configuration in NGC 55, located in the south-eastern part of the main disk (as shown in Figure 1). Initial observations were obtained in 2013 October, with additional data taken in 2014 September as part of back-up observations during a different part of the GTO programme. Unfortunately the conditions in the 2014 run did not lead to improvements on the 2013 data, and these observations are not considered further here.

The observations consisted of a total of 20×600 s integrations, where object exposures (O) and sky-offset exposures (S) interleaved in a O, S, O pattern; taken over the nights of 2013 October 14 and 15, in seeing conditions of $0''.8$ to $1''.2$. In addition, on each night a standard set of KMOS calibration files was obtained as well as observations of a standard star for telluric correction. HIP 3820 (B8 V; Houk 1978) was observed using the 24-arm telluric template (KMOS_spec_acq_stdstarscipatt). However, on 2013 October 14, this OB was interrupted and could not be repeated owing to operational issues, hence several of the IFUs were not observed with the 24-arm template.

Differences in the quality of the data and in the actual execution of the observations must all be taken into account when the data is reduced. The delivered spectral resolutions of our data (from analysis of the relevant arc calibration frames) are summarised in Table 2, where changes in the spectral resolution are principally the result of differences in rotator angles of the Nasmyth axis. These were taken into account when combining exposures from different nights by degrading the spectra to the lowest effective resolving power (using a simple Gaussian filter). For example, spectra for the target in IFU 1 were degraded to a resolving power of 3300 before combining into a master spectrum (the resolution of the Ar $\lambda 1.21430 \mu\text{m}$ line is chosen as this more accurately represents the spectral resolution where the diagnostic lines are present).

The observations were reduced using the recipes provided by the Software Package for Astronomical Reduction with KMOS (SPARK; Davies, R. I. et al. 2013). The standard KMOS/esorex routines were used to calibrate and reconstruct the science and standard-star data cubes as outlined by Davies, R. I. et al. (2013), including correction for the readout column bias as well as enhancing the bad-pixel

Table 2. Measured velocity resolution and resolving power across each detector.

Date	Spectrograph	IFUs	Ne λ 1.17700 μm		Ar λ 1.21430 μm	
			FWHM (km s^{-1})	R	FWHM (km s^{-1})	R
14-10-2013	1	1-8	95.48 ± 2.42	3140 ± 80	90.71 ± 2.09	3305 ± 76
	2	9-16	88.67 ± 1.67	3381 ± 64	86.35 ± 1.84	3472 ± 74
	3	17-24	82.89 ± 1.81	3617 ± 79	80.56 ± 2.11	3721 ± 97
15-10-2013	1	1-8	95.48 ± 2.46	3140 ± 81	90.78 ± 2.12	3302 ± 77
	2	9-16	88.91 ± 1.66	3371 ± 63	86.30 ± 1.85	3473 ± 74
	3	17-24	82.96 ± 2.14	3612 ± 76	80.77 ± 2.14	3712 ± 98

mask following Turner et al. (in prep.). Using the reconstructed data cubes the pipeline was used to extract science and sky spectra in a self-consistent way for all exposures.

Sky subtraction was performed using the ESO SKYCORR package (Noll et al. 2014). SKYCORR is an instrument independent tool that applies a scaling to a sky spectrum given a pair of target and sky spectra in order to more accurately match the sky lines in the target spectrum and hence, provide a more optimised sky subtraction. This works by adapting the reference sky spectrum to correct for differences as a result of temporal and spatial airglow variability. This software is specifically designed for observations at Cerro Paranal and has been shown to be an effective tool for various science goals (e.g. Noll et al. 2014; Gazak et al. 2015; Fossati et al. 2016; La Barbera et al. 2016).

Telluric correction is performed on each sky-subtracted spectrum (before combination) using the method described in full by Patrick et al. (2015). Briefly, additional corrections are made to the standard KMOS/esorex method of telluric correction by correcting for potential offsets between the wavelength solutions of the science and telluric spectra using an iterative cross-correlation approach. In addition, a simple scaling is applied to the telluric spectrum in order to more accurately match the telluric absorption in the science spectrum. Once these additional corrections have been implemented, the science spectra are divided through by the telluric spectrum to remove the telluric contamination.

To combine the fully calibrated and corrected spectra from each night, the spectra are degraded to the lowest resolving power measured for their respective IFUs. Once each set of spectra have a constant resolution, any differences in the wavelength solution are corrected using an iterative cross-correlation approach where each spectrum is corrected to the wavelength solution of a single reference spectrum, for each target. The choice of the reference spectrum for each target is important as, if a poor-quality spectrum (with strong residuals from the sky or telluric correction) were selected, there could be an alignment of the residuals leading to a spurious signal when combined. To avoid this, the highest-quality spectrum for each target is selected as the reference spectrum. In practise, this was typically the fourth exposure from the night of 2013 October 15.

Over an individual night there were generally not significant shifts, so this procedure mainly corrects for differ-

ences arising between each night. Once this correction is implemented all spectra were combined using a simple median combine. This simple method is preferred to something more sophisticated as there were significant sky- and telluric-correction residuals present in many of these spectra, the impact of which was minimised when taking the median of the data.

4 RESULTS AND DISCUSSION

4.1 Radial Velocities

To measure radial velocities, the accuracy of the wavelength solution is vital. For this reason – for the radial-velocity analysis – the data is reduced using a slightly different approach to the one outlined in Section 3. Here, the KMOS/esorex pipeline is used to perform the sky subtraction and combine the frames. After this step, the accuracy of the wavelength solution provided by the KMOS pipeline for each target spectrum (before telluric correction) is checked with a reference telluric spectrum using an iterative cross-correlation approach.

After correction for any shifts in the telluric lines, an initial (stellar) radial velocity was estimated via cross-correlation with a model stellar spectrum over the 1.16–1.21 μm region. Using this estimate as an initial guess, radial velocities are independently measured for several strong spectral features within this region. The final radial velocity is an average of the measurements made using the individual spectral features, where the dispersion defines the uncertainty on the measurement. This method has been shown to work well on stellar spectra from KMOS (Lapenna et al. 2015; Patrick et al. 2015, 2016). This method is preferred to the result using the cross-correlation of the whole 1.16–1.21 μm region as residual reduction features can act to perturb this estimate on large scales, whereas this is more easily identified (by eye) using smaller, well-defined spectral features. Heliocentric corrections were calculated using ESO’s Airmass calculator.¹

Estimated radial velocities for each night are listed in Table 4 and an average is taken for each target. Uncertainties quoted on the average are the standard deviation of

¹ <https://www.eso.org/sci/observing/tools/calendar/airmass.html>

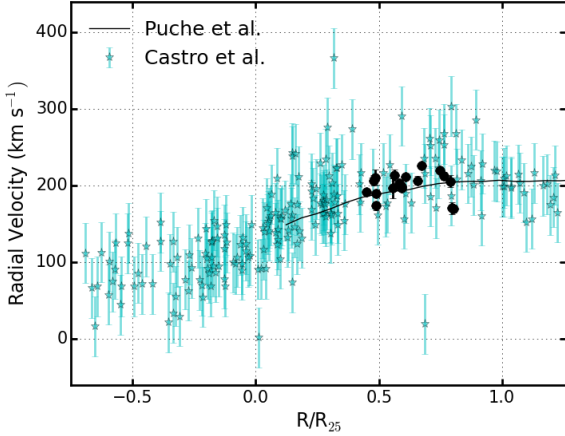


Figure 3. Radial velocities for the KMOS RSGs (black points) shown against projected radius from the centre of NGC 55 as defined by the Two Micron All Sky Survey (2MASS; [Skrutskie et al. 2006](#)) scaled by $R_{25} = 16.2 \pm 0.4$ arcmin ([de Vaucouleurs et al. 1991](#)). Blue stars show data for ~ 200 BSGs in NGC 55 from [Castro et al. \(2008\)](#), shown with 50% transparency to highlight densely populated areas) alongside the rotation curve of NGC 55 (black solid line; [Puche et al. 1991](#)).

the measurements on each night. Three targets have been excluded from this radial velocity analysis (and are not listed in Table 4) based on their spectral appearance and unreliable, inconsistent radial-velocity estimates – owing to reduction residuals.

Comparing the estimated velocities to previous measurements we find good agreement with velocities measured for ~ 200 BSGs in NGC 55 by [Castro et al. \(2008\)](#), as well as with measurements of the velocity from the H I gas ([Puche et al. 1991](#)). The estimated radial velocities as a function of the de-projected galactocentric distance are shown in Figure 3, where previous measurements are also shown for comparison. The radius at which the surface brightness first reaches 25 mag/arcsec² in the *B*-band is shown for scale ($R_{25} = 16.2 \pm 0.4$ arcmin [de Vaucouleurs et al. 1991](#)). We find no evidence for a systematic offset between the measurements of [Castro et al. \(2008\)](#) and those measured in this study. The de-projected radius is calculated by assuming the geometrical model defined by [Puche et al. \(1991\)](#) and updated by [Westmeier et al. \(2013\)](#), i.e. with an inclination angle $i = 78 \pm 4^\circ$ and a position angle $\phi = 109^\circ$.

4.2 Stellar Parameters

Stellar parameters are estimated for each target using the *J*-band analysis technique (given in Table 3). This technique is described and tested in detail by [Davies et al. \(2010, 2015\)](#) and applied to KMOS data by [Patrick et al. \(2015\)](#); [Gazak et al. \(2015\)](#); [Lardo et al. \(2015\)](#) and [Patrick et al. \(2016\)](#). This analysis technique uses a grid of synthetic spectra extracted from stellar model atmospheres to estimate overall metallicity ($[Z] = \log(Z/Z_\odot)$), effective temperature (T_{eff}), surface gravity ($\log g$) and microturbulent velocity (ξ). This technique is tailored specifically to the resolution of KMOS spectra, and with a $S/N \geq 100$ metallicities can be estimated

to a precision of ± 0.10 dex. The range in the parameters used are applicable for RSGs and span $-1.0 \leq [Z] \leq 1.0$, $3400 \leq T_{\text{eff}} \leq 4400$ K, $-1.00 \leq \log g \leq 1.00$ and $1.0 \leq \xi \leq 5.0$ km s⁻¹.

Observations are compared with synthetic RSG spectra, extracted from MARCS stellar model atmospheres ([Gustafsson et al. 2008](#)), with non-LTE corrections computed for the strongest iron, titanium, silicon and magnesium absorption lines ([Bergemann et al. 2012, 2013, 2015](#)). The synthetic spectra are compared with observations using the reduced χ -squared statistic for the 10 diagnostic absorption lines marked in Figure 4. Best-fit parameters are assessed using a sampling of the posterior probability density function using EMCEE ([Foreman-Mackey et al. 2013](#)).

Prior assumptions are implemented based on the luminosity of each target, combined with an acceptable range in mass, based on their spectroscopic confirmation as RSGs. Luminosities have been calculated with ground-based *I*-band photometry using the bolometric correction of [Davies, B. et al. \(2013\)](#), where extinction is accounted for assuming $E(B-V) = 0.15$ and a distance of 2.34 Mpc ([Kudritzki et al. 2016](#)). At this point, it is important to note that the bolometric correction of [Davies, B. et al. \(2013\)](#) is calibrated for a fixed temperature. This may introduce a small uncertainty (on the order of ± 0.1 dex) in luminosities calculated at the hottest and coolest effective temperatures estimated.

Estimated stellar parameters are listed in Table 3 and the best-fit model spectra are shown with the final reduced science spectra in Figure 4. The average uncertainties on the estimated stellar parameters are significantly larger than those quoted in previous studies using the same technique (e.g. [Gazak et al. 2015](#)), which is owing to the quality of the data obtained for these targets and can be illustrated by comparing Figure 4 with Fig. 4 of [Gazak et al. \(2015\)](#). Despite the low S/N achieved (see Table 3), we are still able to provide reasonable estimates of physical parameters for 14 targets, the first spectroscopically confirmed RSGs within NGC 55.

4.2.1 Metallicities and spatial variations

Assuming no spatial variations in metallicity, the average metallicity of the sample is -0.48 ± 0.13 dex. This value compares well to the average metallicity measured using 12 BSGs in NGC 55 from [Castro et al. \(2012, \$-0.40 \pm 0.13\$ \)](#), who found no evidence for spatial variations.

[Kudritzki et al. \(2016\)](#) furthered the work on BSGs by providing metallicity measurements for ~ 60 BSGs in NGC 55, increasing the number of targets five-fold and over a larger spatial extent than [Castro et al. \(2012\)](#). [Kudritzki et al. \(2016\)](#) report a metallicity gradient of -0.22 ± 0.06 dex/ R_{25} , predicting a central metallicity of -0.37 ± 0.03 dex. Using this gradient, for the average R/R_{25} of the RSG sample presented here ($R/R_{25} \approx 0.6$), this relationship predicts $[Z] = -0.52$ dex, in excellent agreement with the average metallicity of the current sample.

Figure 5 displays the estimated metallicities shown as a function of the de-projected radial distance from the centre of the galaxy as defined by the Two Micron All Sky Survey (2MASS; [Skrutskie et al. 2006](#)). The RSG results are shown in black circles and results from [Kudritzki et al. \(2016\)](#) and

Table 3. Physical parameters determined for the KMOS targets in NGC 55.

Target	IFU	S/N	ξ (km s ⁻¹)	[Z]	log <i>g</i>	<i>T</i> _{eff} (K)
NGC55-RSG19	6	35	3.9 ± 0.7	-0.23 ± 0.22	-0.8 ^{+1.2} _{-0.3}	4260 ⁺⁸⁰ ₋₂₁₀
NGC55-RSG24	10	30	4.2 ± 0.8	-0.43 ± 0.32	-0.4 ^{+1.0} _{-0.4}	3920 ⁺³³⁰ ₋₃₇₀
NGC55-RSG25	8	30	3.3 ± 1.1	-0.65 ± 0.32	0.3 ^{+0.3} _{-1.0}	3480 ⁺³⁷⁰ ₋₃₀
NGC55-RSG26	4	25	3.1 ± 1.0	-0.59 ± 0.32	-0.4 ^{+0.9} _{-0.5}	3890 ⁺²⁸⁰ ₋₃₂₀
NGC55-RSG30	3	25	3.6 ± 1.0	-0.49 ± 0.32	0.4 ^{+0.2} _{-1.0}	3660 ⁺³⁶⁰ ₋₁₈₀
NGC55-RSG35	12	30	4.2 ± 0.6	-0.50 ± 0.30	-0.2 ^{+0.5} _{-0.7}	3810 ⁺³¹⁰ ₋₂₅₀
NGC55-RSG39	14	30	3.1 ± 0.9	-0.27 ± 0.26	-0.8 ^{+1.1} _{-0.1}	3830 ⁺²²⁰ ₋₂₇₀
NGC55-RSG43	24	25	3.5 ± 0.9	-0.40 ± 0.29	0.1 ^{+0.3} _{-0.9}	3680 ⁺³⁹⁰ ₋₁₆₀
NGC55-RSG46	22	30	2.7 ± 0.9	-0.50 ± 0.32	0.4 ^{+0.2} _{-1.0}	3950 ⁺³⁰⁰ ₋₄₉₀
NGC55-RSG57	1	35	3.8 ± 0.8	-0.56 ± 0.32	0.1 ^{+0.3} _{-0.3}	3540 ⁺¹⁵⁰ ₋₃₀
NGC55-RSG58	15	30	3.2 ± 1.0	-0.46 ± 0.31	0.1 ^{+0.3} _{-0.9}	3610 ⁺³²⁰ ₋₁₅₀
NGC55-RSG65	17	30	3.5 ± 0.9	-0.54 ± 0.31	-0.6 ^{+0.8} _{-0.3}	3910 ⁺³³⁰ ₋₃₆₀
NGC55-RSG71	20	25	2.6 ± 1.1	-0.71 ± 0.28	0.4 ^{+0.3} _{-1.0}	3560 ⁺²³⁰ ₋₁₂₀
NGC55-RSG73	19	25	3.5 ± 0.9	-0.38 ± 0.30	0.2 ^{+0.4} _{-0.9}	3920 ⁺²⁷⁰ ₋₃₄₀

Castro et al. (2012) are shown in red and blue squares respectively.

Using the RSG data we find a metallicity gradient of -0.49 ± 0.32 dex/ R_{25} (-0.044 ± 0.029 dex/kpc; assuming $R_{25} = 11.0$ kpc). The gradient is determined using a weighted orthogonal distance regression method (scipy.odr), that minimises the sum of the squared weighted orthogonal distances from the observations to a model, taking into account the uncertainties in the de-projected radius (abscissa) and metallicity measurement (ordinate).

This result provides an independent measurement of the recent metallicity gradient estimated by Kudritzki et al. (2016) and predicts a central metallicity for NGC 55 of -0.16 ± 0.20 dex in reasonable agreement with previous estimates. The metallicity gradient estimated using the RSG data has larger uncertainties as a result of the clustered nature of the RSGs at around $\sim 0.6 R_{25}$, whereas the BSG data spans a much larger galactocentric range (as demonstrated by Figure 3). In addition, the individual RSG metallicity measurements are also less secure than the BSG results, thus also increasing the uncertainty on the inferred gradient.

Kudritzki et al. (2016) used a slightly different method to calculate the BSG metallicity gradient. To accurately compare the results we recalculate the metallicity gradient of Kudritzki et al. (2016) with our method and find -0.23 ± 0.06 dex/ R_{25} , in excellent agreement with their result.

Directly comparing the results of these measurements is valid as BSGs and RSGs are closely related in terms of stellar evolution. These stars are predicted to be different stages in the evolution of a single star with initial mass $> 8 M_{\odot}$, and as such have very similar ages. It is important to stress that the RSG results presented here and the BSG results (Castro et al. 2012; Kudritzki et al. 2016) are completely independent measures of stellar metallicity using different types of stars, different stellar model atmospheres, different instrumentation and different wavelength regimes to make these measurements. As such, the agreement between the two sets of results is encouraging and further validates the use of RSGs as effective tools with which to measure extragalactic abundances.

In addition, Magrini et al. (2017) analysed 25 H II re-

gions using the so-called ‘direct’ and ‘strong-line’ emission line methods, yielding abundances of various elements over a similar spatial extent to the blue and red supergiant stars in NGC 55. As H II regions are the birthplace of young massive stars, their abundances should closely match that of their RSG and BSG counterparts. Indeed, this is demonstrated in Gazak et al. (2015) for NGC 300 (the companion galaxy to NGC 55), where the abundance gradients estimated for RSGs, BSGs and H II regions are in remarkable agreement. However, Magrini et al. (2017) found no evidence for a gradient in NGC 55, using the same de-projection and regression analysis as Kudritzki et al. (2016) and this study. A similar result has previously been reported in the LMC where a metallicity gradient has been detected in the asymptotic giant branch population of the LMC (Cioni 2009; Feast et al. 2010), but not with abundances estimated via H II region abundances (Pagel et al. 1978).

The reason for this discrepancy is, at present, unclear. In NGC 55, all three studies had the precision to measure this gradient (even if somewhat ambiguously relying on solely the RSG results), and used consistent methods to estimate this relationship. This rules out inaccuracies in the geometric model (for example, additional structure that is not taken into account), as this would be systematic in all three studies. Additional, more accurate RSG metallicities across a larger spatial extent of NGC 55 are required to reassess this interesting problem.

4.2.2 Stellar Evolution

Luminosities are calculated using the bolometric correction of Davies, B. et al. (2013) at distance of 2.34 ± 0.11 Mpc. A Hertzsprung–Russell (H-R) diagram of our targets is shown in Figure 6, using temperatures and luminosities estimated in Section 4, compared with SMC-like evolutionary tracks (Brott et al. 2011). Results for 15 RSGs in NGC 300 are shown in green for comparison (Gazak et al. 2015). By studying this figure, one notices two interesting features: 1. There appears to be a different distribution of temperatures between the sample presented here and that of NGC 300. 2. A small systematic offset in the average luminosities of the two samples.

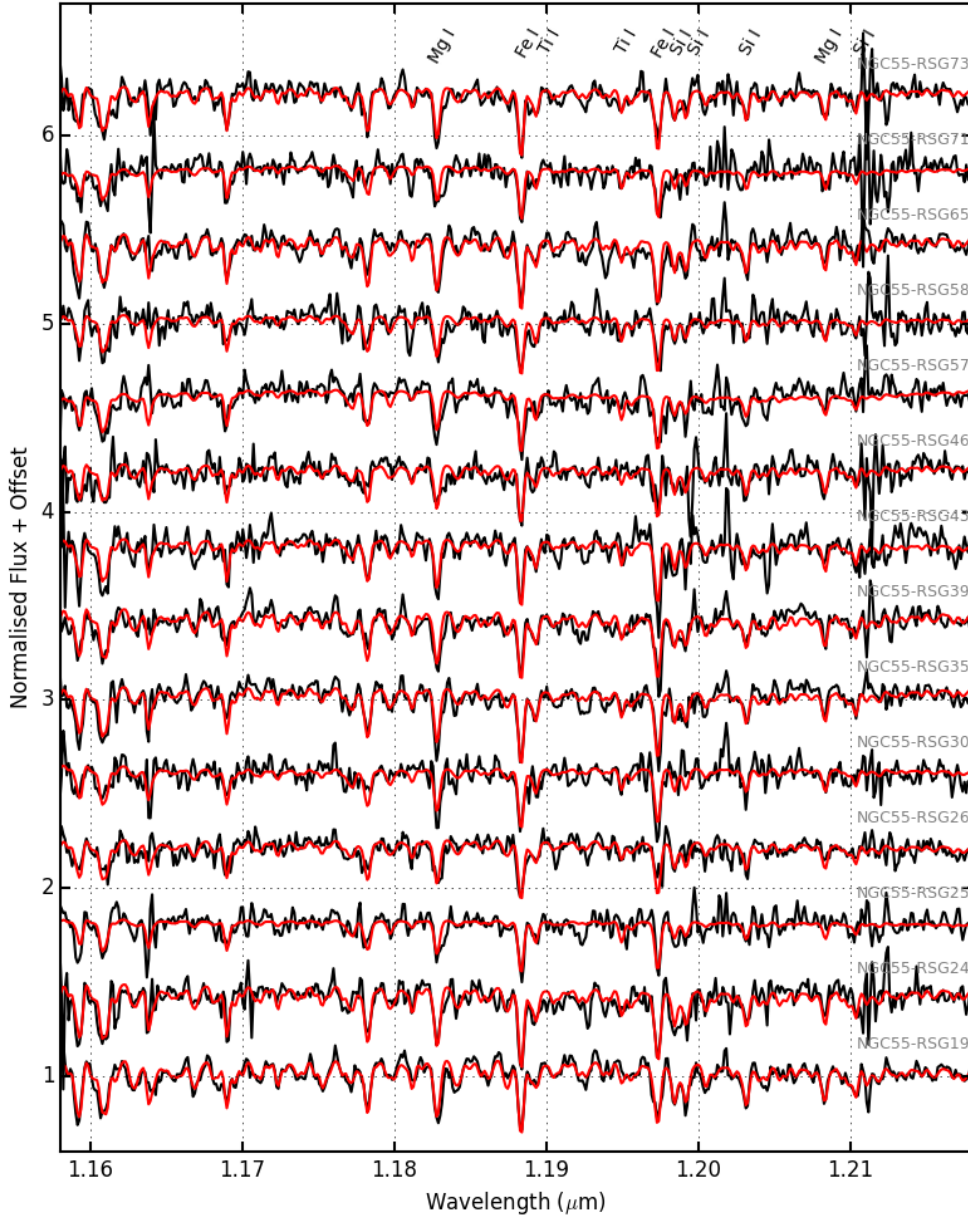


Figure 4. Observed and best-fit model spectra of RSGs in NGC 55 (black and red lines, respectively). The lines used for the analysis, from left-to-right by species, are Fe I $\lambda\lambda$ 1.188285, 1.197305; Mg I $\lambda\lambda$ 1.182819, 1.208335; Si I $\lambda\lambda$ 1.198419, 1.199157, 1.203151, 1.210353; Ti I $\lambda\lambda$ 1.189289, 1.194954.

The distribution of temperatures of the NGC 55 sample is skewed towards lower temperatures where 7/15 targets have $3600 < T_{\text{eff}} < 3800$ K, in contrast to 2/27 in the NGC 300 sample.² Likewise, in the NGC 300 sample, 9/27 targets have $4200 < T_{\text{eff}} < 4400$ K, whereas 1/15 NGC 55 fall within this temperature range. However, we caution that the uncertainties on the NGC 55 data make a statistical comparison of the distribution of these data sets complicated. The weighted mean and standard deviation for the two samples

(NGC 55: 3765 ± 256 K and NGC 300: 4164 ± 173 K), highlights a $\sim 2\sigma$ discrepancy between the means of the distributions.

The differences in these distributions could be accounted for by selection effects, as we do not select unbiased samples in these studies. Unlike NGC 55, NGC 300 has a face-on orientation and the sample from [Gazak et al. \(2015\)](#) is selected over a larger range of galactocentric distance. However, the discrepancy can likely be accounted for by the large uncertainties on the NGC 55 data. Additional data are required to investigate this further.

To ascertain whether or not this difference between the populations is genuine, we revisited results for RSGs

² Note that not all of the 27 RSGs in [Gazak et al. \(2015\)](#) have estimates of luminosity, and hence, some do not appear in Figure 6.

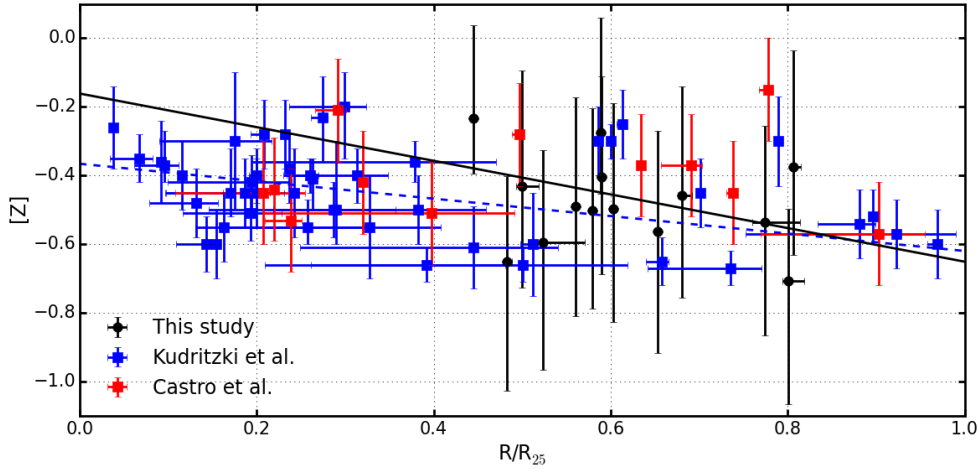


Figure 5. Metallicities for KMOS RSGs (black points) shown against de-projected radius from the centre of NGC 55 as defined by the Two Micron All Sky Survey (Skrutskie et al. 2006) scaled by $R_{25} = 16.18$ arcmin (Karachentsev et al. 2004). The average metallicity of the KMOS RSGs is $[Z] = -0.48 \pm 0.13$ dex. Results for blue supergiant stars (BSGs) from Kudritzki et al. (2016) and Castro et al. (2012) are shown with red and blue squares respectively. The blue dashed line indicates the metallicity gradient calculated for BSGs of Kudritzki et al. (2016), with the equation $y = (-0.25 \pm 0.07)x - (0.37 \pm 0.03)$. The black solid line indicates the metallicity gradient calculated for the RSG targets, with the equation $y = (-0.48 \pm 0.32)x - (0.16 \pm 0.20)$. The larger uncertainties on the RSG fit originate in the smaller coverage in de-projected radius and the larger uncertainties on the RSG metallicities.

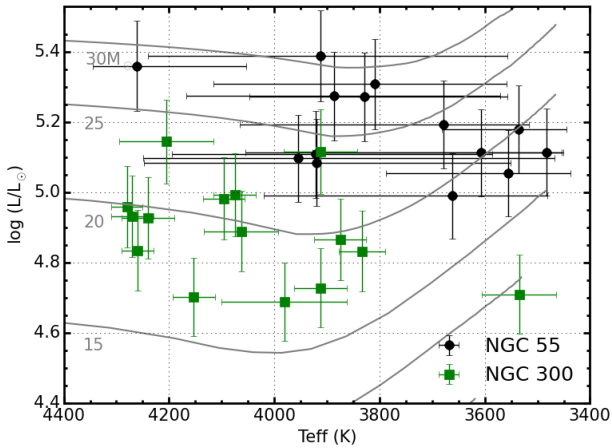


Figure 6. Hertzsprung–Russell diagram for 15 RSGs in NGC 55 shown in black circles. Green squares indicate results from 15 RSGs in NGC 300 from Gazak et al. (2015) for comparison. Solid grey lines show LMC-like metallicity evolutionary models including rotation (Brott et al. 2011). Results from Gazak et al. (2015) in NGC 300 are shown in green for comparison.

in Perseus OB-1 (Gazak et al. 2014), the Magellanic Clouds (Davies et al. 2015; Patrick et al. 2016) and NGC 6822 (Patrick et al. 2015); all of which have temperatures estimated using the same technique. In general, these results have narrower temperature distributions than NGC 55 with average temperatures warmer than that of NGC 55 and cooler than in NGC 300. The six stars in the NGC 55 sample with $T_{\text{eff}} < 3700$ K, appear to be cooler than their counterparts in the other galaxies studied. As mentioned previously, all of the stars in the NGC 55 sample have

significant uncertainties, which make a meaningful comparison difficult.

The observed temperature distribution can be reproduced by stellar evolutionary models by varying the metallicity of the models, in general, higher metallicity models produce lower RSG temperatures. However, the width of the temperature distribution for the NGC 55 targets can likely be attributed to the uncertainties involved in their measurements.

A difference in the luminosity of RSG populations in a given galaxy would imply a difference in the Humphreys–Davidson limit (Humphreys & Davidson 1979) between the different galaxies or a difference in the age of the stellar populations (i.e. the most massive/youngest RSGs of the population will have already exploded as supernovae). However, both galaxies are known to host a significant population of young and old stars at different galactocentric radii and no evidence in the literature for a truncation of star formation in either galaxy is found. In addition, there is no motivation for assuming differences in the Humphreys–Davidson limit.

The luminosities calculated by Gazak et al. (2015) are calculated using the *HST* F814W filter without correcting for the effects of extinction. To more accurately compare luminosities of the two samples we have re-calculated their luminosities assuming $E(B-V) = 0.12$ and $R_V = 3.1$ (Kudritzki et al. 2008). Figure 6 displays these results using this simple extinction correction. However, Kudritzki et al. (2008) note that extinction varies significantly across NGC 300 and can be up to $E(B-V) = 0.24$. Even if we assume that all NGC 300 targets have $E(B-V) = 0.24$ this cannot fully account for the observed offset. The use of the *HST* F814W filter, as opposed to the *I* filter, for the NGC 300 sample introduces an offset of $\sim -0.02 \log L/L_{\odot}$, which contributes a small amount to the difference between the samples.

Another contributing factor may be that the extinction correction used for the NGC 55 targets, $E(B-V) = 0.15$,

which is calculated from the mean of the values from Kudritzki et al. (2016), may be a slight overestimate. This is a result of the differences in the spatial distribution of the RSG and BSG targets i.e. the majority of BSG targets lie at a smaller galactocentric distance than the RSG studied here. If our extinction correction is too severe, this would result in slightly overestimated luminosities for our RSG targets.

The selection criteria used here and by (Gazak et al. 2015) both selected targets in the magnitude range $17 < I < 19$ and at the time it was assumed that both galaxies were at roughly similar distances (~ 1.9 Mpc; Gieren et al. 2005, 2008). However, since then Kudritzki et al. (2016) have argued that NGC 55 is at a larger distance. The effect of this is that, in this study, we have systematically selected more luminous RSGs in NGC 55 compared with NGC 300. Therefore, the fact that we have found that the RSGs in NGC 55 are more luminous, is circumstantial evidence in support of the distance measurement of Kudritzki et al. (2016). In addition, when comparing the luminosities in Figure 6 to that of other samples of RSGs, using the same bolometric correction (that of Davies, B. et al. 2013), we find that both samples fall within the range of expected luminosities for RSGs.

In summary, selection effects and variable extinction within NGC 300 and NGC 55 appear to account for the small systematic offset in luminosities between the two samples.

Interestingly, there appears to be a relationship between the temperature and luminosity of the NGC 55 and NGC 300 targets, where higher temperature targets have larger luminosities. This is in stark contrast to the relationship reported in the literature Dorda et al. (2016, and see Davies, B. et al. 2013), where later spectral types correspond to more luminous stars. In addition, this is at odds with the results of Patrick et al. (2015), who find no significant correlation between luminosity and temperature of 11 RSGs in NGC 6822 (a Local Group dwarf irregular galaxy). If the relationship in Figure 6 is real, then one would also expect this relationship to be apparent in Figure 2. By analysing the observed targets in this figure, there appears to be no significant relationship between colour and magnitude.

The explanation to observed trends in Figure 6, may lie in the method used to calculate the luminosities of these targets, as we only have a small number of photometric data points available. As mentioned earlier, the bolometric correction used here is calibrated at a fixed temperature. Therefore at the most extreme temperatures in our sample, the calculated luminosities may include a small systematic offset (on the order of ± 0.1 dex) towards larger (smaller) luminosities at warmer (cooler) temperatures. To unambiguously define this relationship in NGC 55 requires a larger sample of RSGs with more accurate stellar parameters over a larger spatial scale.

5 CONCLUSIONS

We have presented KMOS spectroscopy for 18 RSGs in the Sculptor Group galaxy NGC 55. Radial velocities are calculated for each epoch and are shown to agree well with measurements for hot massive stars and H I gas, where all targets with reliable radial-velocity measurements are con-

sistent with membership of NGC 55: confirming their nature as supergiants.

Stellar parameters are estimated for 14 targets with the highest-quality observations using the *J*-band analysis technique, which uses a grid of synthetic spectra extracted from state-of-the-art stellar model atmospheres with corrections for non-LTE in the strongest stellar absorption lines in a narrow spectral window. The results of this study confirm the low-metallicity nature of NGC 55 and together with the recent BSG results of Kudritzki et al. (2016), confirm the stellar metallicity gradient. A metallicity gradient of -0.48 ± 0.32 dex/ R_{25} is identified using solely the RSG data, in good agreement with recent estimates of the metallicity gradient using BSG data. The large uncertainties on this gradient are owing to the fact that the RSGs are clustered at a radius of $\sim 0.6 R_{25}$. Interestingly, contemporary metallicity measurements in this galaxy using nebular abundances from H II regions do not follow the same trend, potentially indicating unexpected differences between stellar and nebular abundances in NGC 55, which warrant further investigation.

Luminosities are calculated for our RSG targets and we comment on the relationship between luminosity and temperature in this galaxy, as well as the temperature distribution of the RSGs. The estimated luminosities of RSGs in NGC 55 are compared with those in NGC 300 and we identify a small offset in the luminosities of these studies. In this study, we have adopted the same selection criteria as in NGC 300 (assuming that the two galaxies are at the same distance), therefore, the observed offset is expected if NGC 55 is actually at a larger distance, as reported by Kudritzki et al. (2016).

NGC 55 and its twin galaxy NGC 300 are a fantastic laboratory to test theories of stellar and galactic evolution outside of the Local Group of galaxies. This study presents a first look at metallicities estimated from RSGs in NGC 55 using KMOS spectroscopy in order to study its massive-star population. To determine some of the intriguing results of this initial study more accurately we must acquire additional, higher S/N near-IR spectroscopic observations over the full spatial extent of this galaxy.

ACKNOWLEDGEMENTS

The authors would like to thank the anonymous referee for helpful suggestions that have improved this publication significantly. LRP would like to thank Ignacio Negueruela and Ross McLure for commenting on an earlier draft of this paper. Based on observations collected at the European Organisation for Astronomical Research in the Southern Hemisphere under ESO programme 092.B-0088(A). Support from the Ideas Plus grant of the Polish Ministry of Science and Higher Education IdP II 2015 0002 64 is also acknowledged.

REFERENCES

- Bergemann M., Kudritzki R.-P., Plez B., Davies B., Lind K., Gazak Z., 2012, *ApJ*, **751**, 156
- Bergemann M., Kudritzki R.-P., Würl M., Plez B., Davies B., Gazak Z., 2013, *ApJ*, **764**, 115
- Bergemann M., Kudritzki R.-P., Gazak Z., Davies B., Plez B., 2015, *ApJ*, **804**, 113

- Brott I., et al., 2011, *A&A*, **530**, A115
- Castro N., et al., 2008, *A&A*, **485**, 41
- Castro N., et al., 2012, *A&A*, **542**, A79
- Cioni M.-R. L., 2009, *A&A*, **506**, 1137
- Dalcanton J. J., et al., 2009, *ApJS*, **183**, 67
- Davidge T. J., 2005, *ApJ*, **622**, 279
- Davies, B. et al., 2013, *ApJ*, **767**, 3
- Davies, R. I. et al., 2013, *A&A*, **558**, A56
- Davies B., Kudritzki R.-P., Figer D. F., 2010, *MNRAS*, **407**, 1203
- Davies B., Kudritzki R.-P., Gazak Z., Plez B., Bergemann M., Evans C., Patrick L., 2015, *ApJ*, **806**, 21
- Dorda R., Negueruela I., González-Fernández C., Tabernerero H. M., 2016, *A&A*, **592**, A16
- Engelbracht C. W., et al., 2004, *ApJS*, **154**, 248
- Evans C. J., et al., 2011, *A&A*, **527**, A50
- Feast M. W., Abedigamba O. P., Whitelock P. A., 2010, *MNRAS*, **408**, L76
- Ferguson A. M. N., Wyse R. F. G., Gallagher J. S., 1996, *AJ*, **112**, 2567
- Foreman-Mackey D., Hogg D. W., Lang D., Goodman J., 2013, *PASP*, **125**, 306
- Fossati M., Fumagalli M., Boselli A., Gavazzi G., Sun M., Wilman D. J., 2016, *MNRAS*, **455**, 2028
- Gazak J. Z., Bastian N., Kudritzki R.-P., Adamo A., Davies B., Plez B., Urbaneja M. A., 2013, *MNRAS*, **430**, L35
- Gazak J. Z., Davies B., Kudritzki R., Bergemann M., Plez B., 2014, *ApJ*, **788**, 58
- Gazak J. Z., et al., 2015, *ApJ*, **805**, 182
- Gieren W., Pietrzyński G., Soszyński I., Bresolin F., Kudritzki R.-P., Minniti D., Storm J., 2005, *ApJ*, **628**, 695
- Gieren W., Pietrzyński G., Soszyński I., Bresolin F., Kudritzki R.-P., Storm J., Minniti D., 2008, *ApJ*, **672**, 266
- Gustafsson B., Edvardsson B., Eriksson K., Jorgensen U. G., Nordlund Å., Plez B., 2008, *A&A*, **486**, 951
- Houk N., 1978, Michigan catalogue of two-dimensional spectral types for the HD stars
- Hummel E., Dettmar R.-J., Wielebinski R., 1986, *A&A*, **166**, 97
- Humphreys R. M., Davidson K., 1979, *ApJ*, **232**, 409
- Jerjen H., Freeman K. C., Binggeli B., 1998, *AJ*, **116**, 2873
- Karachentsev I. D., et al., 2003, *A&A*, **404**, 93
- Karachentsev I. D., Karachentseva V. E., Huchtmeier W. K., Makarov D. I., 2004, *AJ*, **127**, 2031
- Kudritzki R.-P., Urbaneja M. A., Bresolin F., Przybilla N., Gieren W., Pietrzyński G., 2008, *ApJ*, **681**, 269
- Kudritzki R. P., Castro N., Urbaneja M. A., Ho I.-T., Bresolin F., Gieren W., Pietrzyński G., Przybilla N., 2016, *ApJ*, **829**, 70
- La Barbera F., Vazdekis A., Ferreras I., Pasquali A., Cappellari M., Martín-Navarro I., Schönebeck F., Falcón-Barroso J., 2016, *MNRAS*, **457**, 1468
- Lapenna E., Origlia L., Mucciarelli A., Lanzoni B., Ferraro F. R., Dalessandro E., Valenti E., Cirasuolo M., 2015, *ApJ*, **798**, 23
- Lardo C., Davies B., Kudritzki R.-P., Gazak J. Z., Evans C. J., Patrick L. R., Bergemann M., Plez B., 2015, *ApJ*, **812**, 160
- Magrini L., Gonçalves D. R., Vajgel B., 2017, *MNRAS*, **464**, 739
- Noll S., Kausch W., Kimeswenger S., Barden M., Jones A. M., Modigliani A., Szyszka C., Taylor J., 2014, *A&A*, **567**, A25
- Pagel B. E. J., Edmunds M. G., Fosbury R. A. E., Webster B. L., 1978, *MNRAS*, **184**, 569
- Patrick L. R., Evans C. J., Davies B., Kudritzki R.-P., Gazak J. Z., Bergemann M., Plez B., Ferguson A. M. N., 2015, *ApJ*, **803**, 14
- Patrick L. R., Evans C. J., Davies B., Kudritzki R.-P., Hénault-Brunet V., Bastian N., Lapenna E., Bergemann M., 2016, *MNRAS*, **458**, 3968
- Pietrzyński G., et al., 2006, *AJ*, **132**, 2556
- Puche D., Carignan C., Wainscoat R. J., 1991, *AJ*, **101**, 447
- Sharples R., et al., 2013, *The Messenger*, **151**, 21
- Skrutskie M. F., et al., 2006, *AJ*, **131**, 1163
- Stasińska G., Comte G., Vigroux L., 1986, *A&A*, **154**, 352
- Tüllmann R., Rosa M. R., Elwert T., Bomans D. J., Ferguson A. M. N., Dettmar R.-J., 2003, *A&A*, **412**, 69
- Webster B. L., Smith M. G., 1983, *MNRAS*, **204**, 743
- Westmeier T., Koribalski B. S., Braun R., 2013, *MNRAS*, **434**, 3511
- Zaritsky D., Kennicutt Jr. R. C., Huchra J. P., 1994, *ApJ*, **420**, 87
- de Vaucouleurs G., 1961, *ApJ*, **133**, 405
- de Vaucouleurs G., de Vaucouleurs A., Corwin Jr. H. G., Buta R. J., Paturel G., Fouqué P., 1991, Third Reference Catalogue of Bright Galaxies. Volume I: Explanations and references. Volume II: Data for galaxies between 0^h and 12^h . Volume III: Data for galaxies between 12^h and 24^h .

Table 4. Summary of VLT-KMOS targets with reliable radial-velocity estimates consistent with NGC 55.

ID	α (J2000)	δ (J2000)	V ^a	I ^a	$F606W$ ^b	$F814W$ ^b	rv (km s ⁻¹)		$\langle rv \rangle$ (km s ⁻¹)	Notes
							14-10-2013	15-10-2013		
NGC55-RSG19	00:15:29.190	-39:14:08.20	19.914	17.731	19.85	17.76	205 ± 4	178 ± 7	192 ± 4	
NGC55-RSG20	00:15:29.520	-39:15:13.00	20.832	18.952	20.86	19.11	194 ± 14	220 ± 5	207 ± 7	Potential blend from <i>HST</i> image
NGC55-RSG24	00:15:31.460	-39:14:46.30	20.612	18.475	20.29	18.38	186 ± 6	194 ± 7	190 ± 5	
NGC55-RSG25	00:15:31.490	-39:14:32.40	20.316	18.394	20.63	18.49	204 ± 12	217 ± 16	211 ± 10	
NGC55-RSG26	00:15:33.160	-39:13:42.00	20.572	17.964	20.35	18.06	174 ± 9	173 ± 8	174 ± 6	
NGC55-RSG28	00:15:36.160	-39:15:29.40	21.001	18.892	20.87	18.97	233 ± 17	161 ± 20	197 ± 13	
NGC55-RSG30	00:15:38.030	-39:14:50.20	20.867	18.730	20.79	18.75	212 ± 10	215 ± 10	214 ± 7	
NGC55-RSG35	00:15:39.260	-39:15:01.70	20.007	17.872	19.78	17.73	202 ± 3	206 ± 4	204 ± 3	
NGC55-RSG39	00:15:40.260	-39:15:01.00	19.654	17.970	20.36	18.19	206 ± 11	192 ± 5	199 ± 6	
NGC55-RSG43	00:15:40.700	-39:14:50.20	19.957	18.183	20.36	18.25	198 ± 6	196 ± 5	197 ± 4	Potential blend from <i>HST</i> image
NGC55-RSG46	00:15:41.640	-39:14:58.80	21.591	18.441	20.85	18.52	228 ± 5	195 ± 6	212 ± 4	Potential blend from <i>HST</i> image
NGC55-RSG57	00:15:45.590	-39:15:16.40	20.010	18.220	–	–	217 ± 10	197 ± 6	207 ± 6	
NGC55-RSG58	00:15:46.270	-39:15:43.20	20.619	18.400	–	–	236 ± 8	216 ± 3	226 ± 4	
NGC55-RSG65	00:15:51.250	-39:16:26.40	19.706	17.653	–	–	224 ± 5	215 ± 4	220 ± 3	
NGC55-RSG69	00:15:55.280	-39:15:00.10	20.470	18.666	–	–	231 ± 5	195 ± 9	213 ± 5	
NGC55-RSG70	00:15:56.310	-39:16:08.60	22.300	18.907	–	–	155 ± 12	187 ± 9	171 ± 8	
NGC55-RSG71	00:15:56.900	-39:15:27.50	20.401	18.559	–	–	197 ± 11	214 ± 11	206 ± 8	
NGC55-RSG73	00:15:57.710	-39:15:41.50	20.489	18.411	–	–	161 ± 7	178 ± 6	170 ± 5	

a Ground-based data from the Araucaria Project (Pietrzyński et al. 2006), with typical photometric uncertainties of 0.075 and 0.016 mag in the V - and I -bands, respectively.

b *HST* ANGST photometry from Dalcanton et al. (2009), with typical uncertainties of 0.12, 0.13 mag in the $F606W$ and $F814W$ bands, respectively.

This paper has been typeset from a $\text{T}_{\text{E}}\text{X}/\text{L}^{\text{A}}\text{T}_{\text{E}}\text{X}$ file prepared by the author.